

Article

Nanoporous Activated Carbon Material from *Terminalia chebula* Seed for Supercapacitor Application

Chhabi Lal Gnawali¹, Lok Kumar Shrestha^{2,3,*} , Jonathan P. Hill² , Renzhi Ma², Katsuhiko Ariga^{2,4} ,
Mandira Pradhananga Adhikari⁵, Rinita Rajbhandari¹ and Bhadra P. Pokharel¹

¹ Department of Applied Sciences and Chemical Engineering, Pulchowk Campus, Institute of Engineering (IOE), Tribhuvan University, Lalitpur 44700, Nepal; chhabig123@ioe.edu.np (C.L.G.); rinita.joshi@pcampus.edu.np (R.R.); bhadrapokharel@ioe.edu.np (B.P.P.)

² Center for Materials Nanoarchitectonics (WPI-MANA), National Institute for Materials Science (NIMS), 1-1 Namiki, Tsukuba 305-0044, Ibaraki, Japan; jonathan.hill@nims.go.jp (J.P.H.); ma.renzhi@nims.go.jp (R.M.); ariga.katsuhiko@nims.go.jp (K.A.)

³ Department of Materials Science, Faculty of Pure and Applied Sciences, University of Tsukuba, 1-1-1 Tennodai, Tsukuba 305-8573, Ibaraki, Japan

⁴ Department of Advanced Materials Science, Graduate School of Frontier Sciences, The University of Tokyo, 5-1-5 Kashiwanoha, Kashiwa 277-8561, Chiba, Japan

⁵ Central Department of Chemistry, Tribhuvan University, Kirtipur, Kathmandu 44613, Nepal; mandira43@hotmail.com

* Correspondence: shrestha.lokkumar@nims.go.jp; Tel.: +81-29-860-4809

Abstract: High-surface-area porous carbon materials with high porosity and well-defined pore structures are the preferred advanced supercapacitors electrode materials. Here, we report the electrochemical supercapacitive performance of novel high-porosity activated carbon materials prepared from biowaste *Terminalia chebula* (Harro) seed stones involving zinc chloride (ZnCl_2) activation. Activation is achieved by mixing ZnCl_2 with Harro seed powder (1:1 *w/w*) followed by carbonization at 400–700 °C under a nitrogen gas atmosphere. The amorphous carbon materials obtained exhibit excellent performance as electrical double-layer capacitor electrodes in aqueous electrolyte (1 M sulfuric acid) due to high specific surface areas (as high as 1382.6 m² g⁻¹) based on well-developed micropore and mesopore structures, and partial graphitic structure containing oxygenated surface functional groups. An electrode prepared using material having the optimal surface textural properties achieved a large specific capacitance of 328.6 F g⁻¹ at 1 A g⁻¹ in a three-electrode cell setup. The electrode achieved a good capacitance retention of 44.7% at a high 50 A g⁻¹ current density and outstanding cycling performance of 98.2% even following 10,000 successive charge/discharge cycles. Electrochemical data indicate the significant potential of *Terminalia chebula* seed-derived porous carbons as high-performance electrode materials for high-energy-storage supercapacitor applications.



Citation: Gnawali, C.L.; Shrestha, L.K.; Hill, J.P.; Ma, R.; Ariga, K.; Adhikari, M.P.; Rajbhandari, R.; Pokharel, B.P. Nanoporous Activated Carbon Material from *Terminalia chebula* Seed for Supercapacitor Application. *C* **2023**, *9*, 109. <https://doi.org/10.3390/c9040109>

Academic Editor: Manuel Fernando Ribeiro Pereira

Received: 10 October 2023

Revised: 8 November 2023

Accepted: 13 November 2023

Published: 14 November 2023



Copyright: © 2023 by the authors. Licensee MDPI, Basel, Switzerland. This article is an open access article distributed under the terms and conditions of the Creative Commons Attribution (CC BY) license (<https://creativecommons.org/licenses/by/4.0/>).

Keywords: *Terminalia chebula* (Harro); ZnCl_2 activation; nanoporous carbons; supercapacitors

1. Introduction

Global energy demands continue to rise due to the continuously increasing world population, deepening the energy crisis and putting further pressure on fossil fuel supplies. The development of advanced energy storage devices based on the use of clean renewable energy sources is thus an urgent requirement to maintain human society. Also, industrialization and urbanization have led to severe energy shortages and environmental pollution. Various biomaterial-based products have been developed to replace fossil fuel-based energy sources because of their low cost, eco-friendliness, excellent multi-dimensional multi-element structures, and sustainability. Lithium-ion batteries and supercapacitors are both commercially viable types of energy storage device, which have found application widely in hybrid electric vehicles, military garment devices, medical devices, and many electrical appliances [1–5]. Supercapacitors have higher power densities than batteries

and also exhibit extremely rapid charge and discharge times as well as excellent cycle stability [6–10].

Supercapacitors, which are commonly referred to as electrical double-layer capacitors (EDLCs), can be used as electrochemical energy devices that accumulate charge in the form of an electrochemical double-layer at the interface between an electrolyte solution and an electrode surface. Activated nanoporous carbon prepared from biomass has been widely applied for supercapacitor electrode applications based on their ultrahigh surface areas, well-developed pore size distributions, low costs, simple preparation methods, excellent electrical conductivity, and high physicochemical stability [11–20]. The specific surface area and the porous structure are key factors in the use of carbon materials as electrodes since their optimization can be used to enhance the specific capacitance [21]. For adsorption and desorption of ions, micropores play the main role with mesopore structure affecting the transmission pathways of electrolyte ions [22]. The consideration of the mesopore structure can be used to increase the ion diffusion so that ions can easily enter into the internal micropores, while macropores function as sites for the accumulation and retention of ions, which can cause buffering. For this reason, the specific capacitance of EDLCs is not related to the micropore characteristics because most of the micropores are not involved in the charge/discharge process [23]. Hence, both mesopores and macropores play an important role in assisting ionic transport leading to reduced transmission times and allowing more micropores to participate in ion adsorption and desorption [24,25].

Biomass-derived porous activated carbons are potential candidates as electrode materials of supercapacitors due to their excellent electrical conductivity and electrochemical stability accompanied by controllable specific surface area and micropore structures [26–36]. However, the selection of the precursor is based on carbon content, cost, availability, and sustainability. Recently, the large-scale, low-cost fabrication of nanoporous activated carbon materials from different biowaste precursors has been developed for the fabrication of electrode materials towards supercapacitor applications. For example, Shrestha et al. [37] have prepared hierarchically porous carbon materials from *Phyllanthus emblica* by chemically activating using KOH. The resulting material has a substantial surface area ($1946 \text{ m}^2 \text{ g}^{-1}$), leading to a large specific capacitance (272 F g^{-1} @ 1 A g^{-1}) with 60% capacitance retention @ 50 A g^{-1} and a remarkably long cycle endurance with 98% activity retained even following 10,000 consecutive charge/discharge cycles. Qing Xu et al. [38] recently reported porous carbon obtained from biomass tar by using thermal activation with potassium acetate at $800 \text{ }^\circ\text{C}$. The resulting carbon material exhibited 310.4 F g^{-1} specific capacitance @ 0.2 A g^{-1} with initial capacitance retention of 91% after 5000 charge/discharge cycles @ 5 A g^{-1} current density. These recent examples highlight the significant potential of biowaste stuffs for the preparation of activated carbon as the electrode material for high-performance supercapacitors [39–45].

In this contribution, the electrochemical supercapacitor performance of novel nanoporous activated carbon materials prepared from *Terminalia chebula* (Harro) seed stones by ZnCl_2 activation is presented. Harro seed stone powder was mixed with ZnCl_2 in 1:1 weight ratio. Samples of the mixture were then carbonized, respectively at 400, 500, 600, and $700 \text{ }^\circ\text{C}$ for four hours under nitrogen atmosphere. The resulting amorphous carbon materials showed good performance as supercapacitor electrode materials in aqueous electrolyte in a three-electrode system. The sample with optimal surface area delivered a large specific capacitance of 328.6 F g^{-1} @ 1 A g^{-1} and good retention of capacitance (44.7% @ 50 A g^{-1}) with an excellent cycle endurance of 98.2% following 10,000 consecutive charge/discharge cycles. These results show the potential of Harro seed as a carbon source for the cost-effective and scale-up production of nanoporous activated carbon materials as high-performance electrode materials for supercapacitor applications.

2. Materials and Methods

2.1. Materials

Terminalia chebula (Harro) fruit was purchased from a local market. Zinc chloride (ZnCl_2 : 99.5%), hydrochloric acid solution (1 M), and sulfuric acid solution (1 M) were purchased from Nacali Tesque Inc. Kyoto, Japan. Millipore filtered water was used for washing and preparing solution.

2.2. Preparation of Nanoporous Activated Carbons

Harro seed stone, a biowaste, was washed several times with distilled water then dried at 50 °C for 24 h. Dried seeds were pulverized and sieved using a 300 μm mesh. The precursor was combined with ZnCl_2 (1:1 *w/w*), and the mixture was carbonized in a tube furnace at 400, 500, 600, and 700 °C under a nitrogen gas flow (120 cc min^{-1}). A 4 h hold time was applied. The obtained materials were treated with 0.1 M hydrochloric acid, then washed using distilled water until the washings were neutral (pH~7). The samples were then dried in a vacuum oven at 100 °C for 6 h. Samples are referred to as HrC_Z400, HrC_Z500, HrC_Z600, and HrC_Z700, where the numbers indicate the temperature of carbonization. Yields were ca. 45.9% (HrC_Z400), 43% (HrC_Z500), 42.7% (HrC_Z600), and 42.7% (HrC_Z700). For comparison, a control sample was prepared by the direct carbonization of the precursor for 4 h at 500 °C and is referred to as HrP_500.

2.3. Characterization

Pyrolytic decomposition and surface functionality of the precursor were investigated by using thermogravimetry and infrared (FTIR) spectrophotometry. Thermogravimetric analyses (TGA) were undertaken using an SII Instrument Model Exstar 600 and FTIR spectra were recorded on a Nicolet 4700, Thermo Electron Corporation, Waltham, MA, USA. Textural properties including total specific surface area, pore size distribution, and pore volume of the activated carbon materials and the reference sample were studied by nitrogen gas adsorption. Nitrogen gas adsorption/desorption isotherms were recorded using a Quantachrome Autosorb-iQ2, Boynton Beach, FL, USA, operated at the liquid nitrogen temperature of 77.35 K in the relative pressure range of 10^{-7} to 1. Pore size distribution profiles were calculated using density functional theory (DFT: for micropores) and the Barrett–Joyner–Halenda method (BJH: for mesopores). Samples (~25 mg) were annealed at 120 °C for 24 h prior to nitrogen adsorption measurements. Powder X-ray diffraction (XRD; Rigaku X-ray diffractometer RINT, Tokyo, Japan, Cu-K α radiation ($\lambda = 0.1541$ nm) operating at $V = 40$ kV and $I = 40$ mA; sample temperature: 25 °C; diffraction angle range from 10 to 50°), Raman scattering spectroscopy (NRS-3100, JASCO, Tokyo, Japan) excitation wavelength of 532.09 nm; acquisition time 30 sec; accumulation for 10 times; laser power of 1.5 μW ; diffraction grating of 1800 l/mm; and objective lens UMPLFL 20 \times were used. Raman data (line shapes) were fitted using Gauss model, and transmission electron microscopy (TEM: JEOL Model JEM 2100F, Tokyo, Japan operating at 200 kV) was employed for structural characterization. Surface pore structure and surface morphology were observed by using scanning electron microscopy (SEM: S-4800, Hitachi Co., Ltd., Tokyo, Japan operated at $V = 10$ kV/ $I = 10$ μA).

2.4. Electrochemical Measurements

Electrochemical supercapacitance performances were studied by using cyclic voltammetry (CV), electrochemical-impedance spectroscopy (EIS), and galvanostatic charge/discharge (GCD) measurements in a three-electrode-cell using an aqueous 1 M H_2SO_4 electrolyte solution. Working electrodes were prepared on a glassy carbon electrode (GCE). Each subject material (4 mg) was suspended in a solvent of water/ethanol 4:1 *v/v* mixture (2 mL) with sonication for 1 h. An aliquot of the resulting suspension (3 μL) was cast on the GCE surface followed by drying at 60 °C for 2 h. An aliquot of Nafion solution (5 μL ; 5% *w/v* in ethanol) was added as a binder. The modified electrode was then dried by warming it at 60 °C (2 h). The mass of active material on each working electrode was calculated to be

6×10^{-3} mg. CV, GCD, and EIS measurements were taken using a CHI 660E workstation (CH Instruments, Inc., Austin, TX, USA) using Ag/AgCl and platinum wire, respectively as reference and counter electrodes. The specific capacitance (C_s) of the electrode materials was calculated from the GCD curves as follows:

$$C_s = \frac{I \cdot t_d}{m \cdot \Delta V} \quad (1)$$

where I (A) is discharge current, t_d (s) is discharge time, m (g) is the mass of active material on the GCE electrode, and ΔV (V) defines the potential window.

3. Results and Discussion

Pyrolytic decomposition and the mass–temperature relationship of the precursor was studied by recording its TGA curve in the range of 25 to 1000 °C under a nitrogen gas atmosphere. Mass loss in three stages (highlighted by dashed dotted arrows) can be seen in the resulting TGA curve (Figure 1a). Weight loss due to the evaporation of water, crystals, or moisture present in the precursor is seen in the first stage in the range of 35–200 °C.

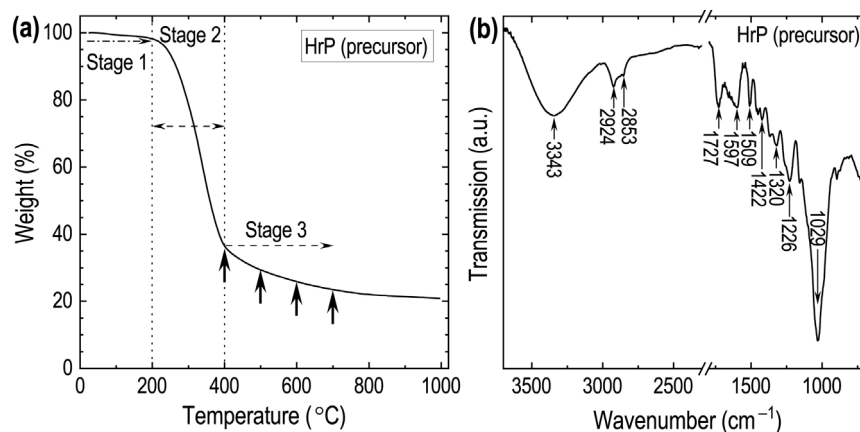


Figure 1. (a) TGA curve; (b) FTIR spectrum of the precursor *Terminalia chebula* seed powder. The upward arrows in panel (a) highlight the carbonization temperatures of the prepared carbon materials.

In the second stage (200–400 °C) a major weight loss occurs that corresponds to the pyrolytic breakdown of hemicellulose and cellulose components with partial decomposition of the lignin content [46]. In the third stage, there is no noticeable weight loss above 400 °C and the carbonization process takes place above 400 °C, indicating that suitable temperatures for the carbonization of Harro seed are above 400 °C.

Functional groups related to the cellulose, hemicellulose, and lignin of precursor powder are clearly visible in the FTIR spectrum of the precursor (Figure 1b). The broad FTIR peak at ~ 3343 cm^{-1} corresponds to the O-H (str.) vibration of the hydroxyl groups, and bands at ~ 2924 and ~ 2853 cm^{-1} are due to the C-H (str.) of alkyl groups [47]. The C=O (str.) of the acetyl groups in cellulose, hemicellulose, and lignin appear at ~ 1727 cm^{-1} . A low-intensity FTIR band at 1593 cm^{-1} is assigned to the C=C (str.) of lignin. Bands at 1422 and 1320 cm^{-1} are assigned to the stretching and bending vibrations of methylene and hydroxy groups in cellulose, respectively [48–50]. Weak absorption bands at 1226 and 1029 cm^{-1} are assigned to aromatic C=C (str.) and C–O (str.) vibrations of the guaiacyl units in lignin, respectively [47–50].

Nitrogen adsorption desorption isotherms of the carbon samples were collected to study their surface textural properties. Adsorption isotherms of the carbon materials prepared at different temperatures of carbonization are shown in Figure 2a. These activated carbon materials adsorb nitrogen strongly at lower relative pressures with obvious hysteresis at higher pressures, leading to isotherms containing type I and type IV behaviors most likely due to their hierarchical micro/mesoporous structures [51]. Large nitrogen adsorption at low relative pressures ($P/P_0 < 0.1$) is due to the filling of micropores. Capillary

condensation occurring in mesopores can be judged from the hysteresis loop in the high relative pressure region [51,52]. Note that an increase in carbonization temperature from 400 to 700 °C leads to an increase in the overall nitrogen adsorption from low to high relative pressure, suggesting an increased abundance of micro- and mesopores in the materials prepared at higher temperatures. The reference carbon sample obtained by direct carbonization without activation (HrP_500) displays type III adsorption isotherm, indicating the absence of porosity, demonstrating the crucial role of the activator ZnCl_2 in the developing porosity of the activated carbons. ZnCl_2 , as a Lewis acid, acts as the dehydrating reagent as it catalyzes the decomposition of lignocellulosic compounds. ZnCl_2 activation is an efficient catalyst for C-O and C-C bond scission. During pyrolysis, ZnCl_2 melts at 290 °C, and above the melting point, it intercalates into the carbon to produce pores. Increasing the pyrolysis temperature causes the zinc oxide chloride hydrate to thermally dehydrate, resulting in the formation of a solid phase of zinc oxide and a gaseous phase of ZnCl_2 . The gaseous phase of ZnCl_2 is diffused into the interior of the biomass to develop the pore network. The carbonized sample is subjected to washing with acid and water; acid removes all the alkali and alkaline earth metals, and water removes all basic and water-soluble components in the carbon that will yield porosity in the carbon structure. The washing process opens the blocking pore entrances to the nitrogen molecules. Figure 2b shows the micropore size distributions obtained by DFT analysis. Figure 2c shows the mesopore distributions obtained from the BJH model. These data verify a hierarchical pore structure of the materials containing both micro and mesopores. The peaks centered at 0.286 nm (Figure 2b) and 3.67 nm (Figure 2c) increase in intensity with increasing carbonization temperature, suggesting increases both in micro- and mesoporosity. Table 1 summarizes the surface textural properties of the materials.

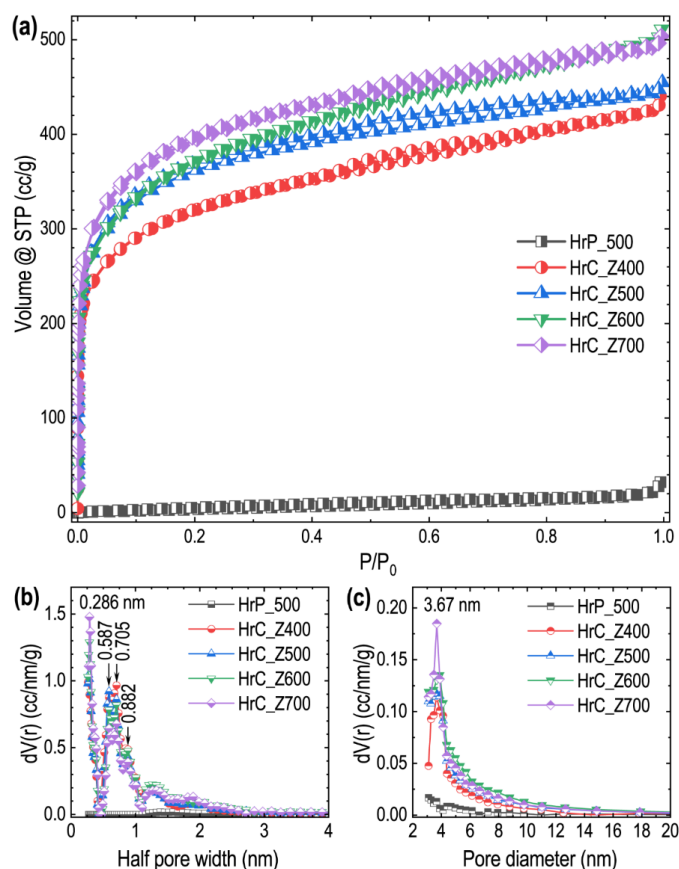


Figure 2. (a) Nitrogen sorption–desorption isotherms; (b) pore size distributions (micropore); and (c) pore size distributions (mesopore) of HrP_500, HrC_Z400, HrC_Z500, HrC_Z600, and HrC_Z700.

Table 1. Textural properties of Harro seed-derived porous carbon materials *.

System	SSA (m ² g ⁻¹)	S _{mic} (m ² g ⁻¹)	S _{mes} (m ² g ⁻¹)	V _p (cm ³ g ⁻¹)	V _{mic} (cm ³ g ⁻¹)	V _{mes} (cm ³ g ⁻¹)	W _p (nm)	D _p (nm)
HrP_500	29.7	12.4	17.3	0.075	0.031	0.044	----	3.1
HrC_Z400	1152.2	1052.9	99.3	0.741	0.602	0.139	0.286	3.67
HrC_Z500	1230.1	1104.4	125.7	0.804	0.627	0.177	0.262	3.66
HrC_Z600	1301.2	1160.3	140.9	0.915	0.707	0.208	0.286	3.67
HrC_Z700	1382.6	1225.8	156.8	0.929	0.697	0.232	0.274	3.66

* SSA = total specific surface area, S_{micro} = surface area of micropore, S_{meso} = surface area of mesopore, V_p = total pore volume, V_{micro} = micropore volume, V_{meso} = mesopore volume, W_p = half pore width, and D_p = pore diameter.

Surface morphologies of Harro seed-derived carbons were observed by using SEM (Figure 3). Low magnification SEM images of all the prepared materials (reference sample and activated samples) show carbon particles of the materials with random shapes and dimensions (Figure 3a,d,g,j,m). Higher magnification SEM images (Figure 3b,c) of the reference sample do not show a porous structure, which aligns with the nitrogen adsorption result. In contrast, a non-uniform macroporous channel-like morphology of the materials is seen in the activated carbon samples (Figure 3e,h,k,n), which is often observed for biomass-derived activated carbons [53–55]. Furthermore, high-resolution SEM images (Figure 3f,i,l,o) show a well-developed mesoporous structure in the activated carbon samples [53–55]. Electronic supporting information contains additional SEM images (ESI: HrP_500 (Figure S1), HrC_Z400 (Figure S2), HrC_Z500 (Figure S3), HrC_Z600 (Figure S4), and HrC_Z700 (Figure S5)). The porosity of the materials seems to increase with carbonization temperature. Note that the pore structure is not well-developed in the directly carbonized sample (Figure 3b,c), suggesting the critical role of the activating agent for the formation of micro/mesopore structures.

The structural characterization of the material (HrC_Z700), having the optimal surface textural properties, was also performed by TEM (Figures 4 and S6). Low-resolution TEM images (Figure 4a–c) show the disordered macro-, meso-, and micropore structures [56]. HR-TEM images (Figure 4d–f) reveal microporous carbon structure having randomly grown graphitic carbon layers [57]. The interlayer spacing of the random carbon layers is ca. 0.357 nm. Note that high temperature carbonization causes the gasification and release of volatile organic compounds, resulting in the formation of micro- and mesopores in the carbon skeleton.

The structure of the porous carbon materials was also studied by using XRD and Raman scattering spectroscopy. Two broad diffraction bands appearing at diffraction angles 24 and 43° (Figure 5a) in the XRD patterns correspond to the (002) and (100) planes of disordered graphitic structures in amorphous carbons, which are usually observed in activated carbons obtained from biomass [58]. XRD patterns of the directly carbonized material contains some low intensity peaks apart from (002) and (100) reflections, which might be due to the presence of impurities. Note that the reference sample was not treated with dilute HCl solution. XRD patterns of the other materials indicate their amorphous structures.

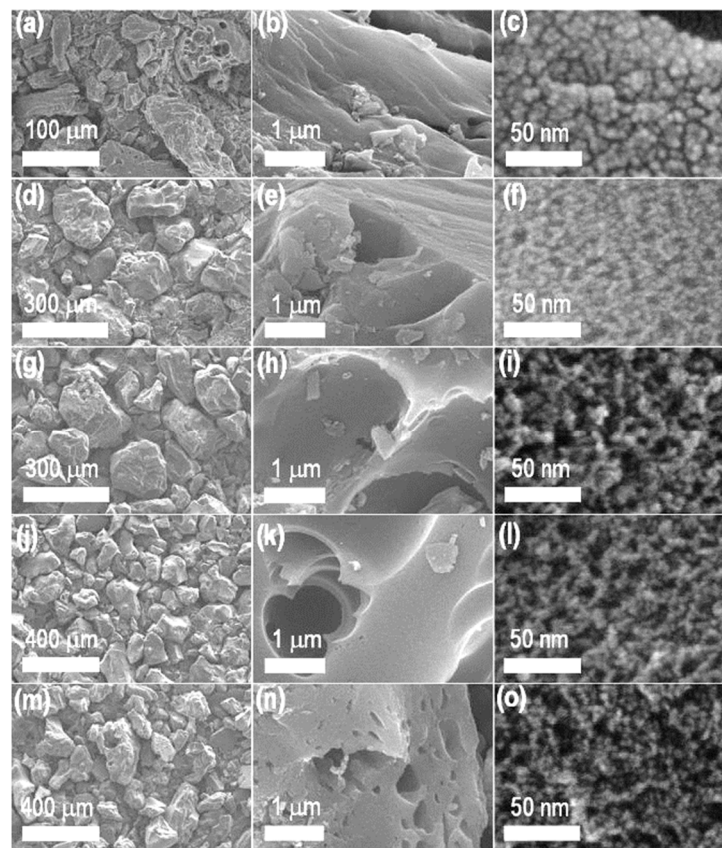


Figure 3. SEM images of (a–c) HrP_500, (d–f) HrC_Z400, (g–i) HrC_Z500, (j–l) HrC_Z600, and (m–o) HrC_Z700.

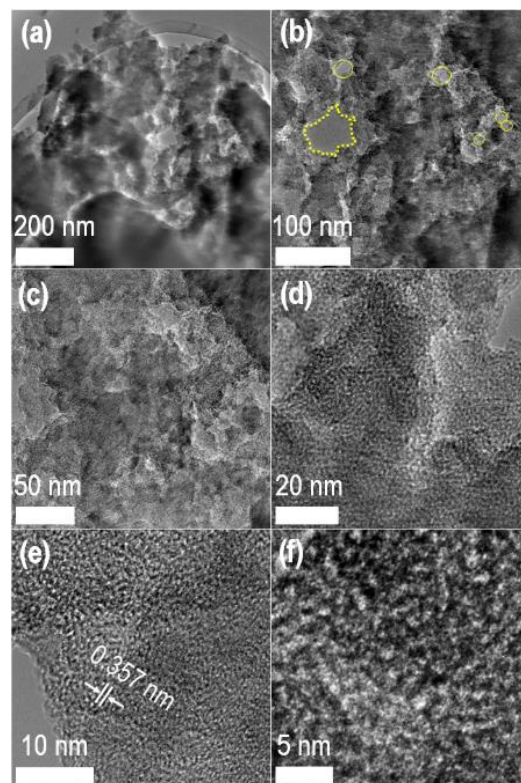


Figure 4. (a–c) TEM and (d–f) HR-TEM images of HrC_Z700. Dotted lines in panel (b) highlights the macropores and solid circles representing mesopores.

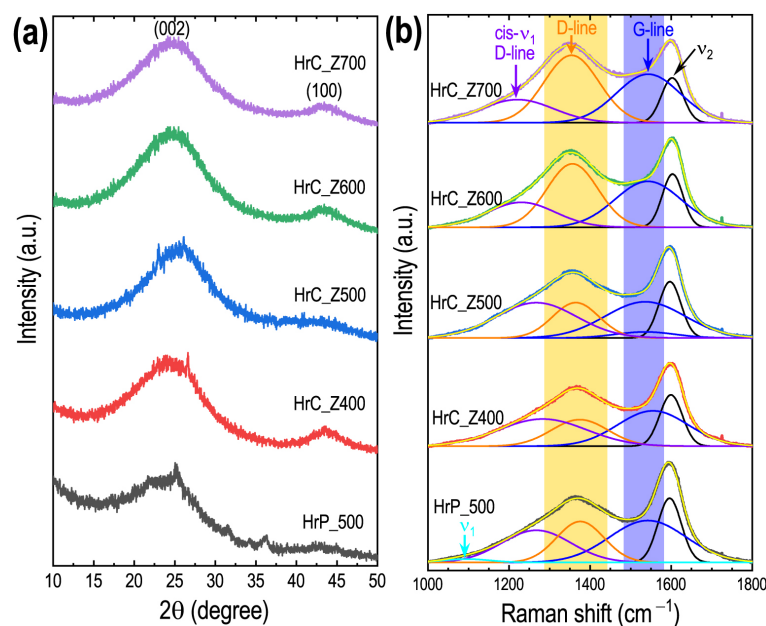


Figure 5. Powder XRD patterns (a), Raman scattering spectra (b) of HrP_500, HrC_Z400, HrC_Z500, HrC_Z600 and HrC_Z700.

Figure 5b shows the experimental Raman scattering spectra of the prepared carbon samples with the fitting components. The Raman spectra exhibit the characteristic of amorphous carbons [59]. Peak fitting components reveal that the directly carbonized reference sample, HrP_500, can be fitted with a small peak at 1100 cm^{-1} corresponding to the polyenic structure. Moreover, all the spectra show amorphous carbon structures with D- and G-lines related to C–C and C=C vibrations [60]. Plateaus in the $1220\text{--}1270\text{ cm}^{-1}$ and $1350\text{--}1375\text{ cm}^{-1}$ regions correspond to the sum of the peaks related to the sum of amorphous carbon associated with D-line and cis-polyacetylene-related C–C vibrations ($\text{cis-}\nu_1$). Peaks at $1540\text{--}1545\text{ cm}^{-1}$ and $1590\text{--}1605\text{ cm}^{-1}$ can be attributed to the G-lines of amorphous carbons and C=C vibrations of polyenes. Note that the intensity of the D-line, which is attributed to the breathing mode of the graphitic structural unit, increases with increasing carbonization temperature from 400 to $700\text{ }^\circ\text{C}$, suggesting the increasing structural defects in the carbon frameworks. The FTIR spectra of the control non-activated material and the chemically activated materials exhibit similar vibrational bands related to C=C (str.) (Figure S7). The band intensity corresponding to surface functional groups decreased due to ZnCl_2 activation and annealing.

Based on their high specific surface areas, well-defined hierarchically micro- and mesoporous structures, and oxygenated surface functional groups, the electrochemical energy storage supercapacitance performances of the activated carbons were studied. Figure 6a shows the CV profiles of these carbon materials, including the reference material at 50 mV s^{-1} . All the electrodes exhibit semi-rectangular CV profiles, inferring a largely EDLC-type behavior, which is commonly observed in carbon-based supercapacitors [61,62]. The non-rectangular-shaped CV curves with weak redox peaks observed at approximately $0.3\text{--}0.4\text{ V}$ can be attributed to a limited contribution of pseudocapacitive behavior to the EDLC. The presence of oxygenated functional groups in the carbon materials contributes to its pseudocapacitance. Note that the total internal current collected in the CV curve of the reference HrP_500 sample is low, but this increases with increasing carbonization temperature. The largest current collection in the HrC_Z700 sample suggests a highest energy storage capacity amongst these materials, which is in line with the surface area, i.e., carbons with higher specific surface area suggests better energy storage properties. CV responses recorded across a wide range of scanning rates ($5\text{--}500\text{ mV s}^{-1}$) for the reference sample, HrP_500 (Figure S8) and the activated carbon samples HrC_Z500 (Figure 6b),

HrC_Z600 (Figure 6c), and HrC_Z700 (Figure 6d) shows that total current output increases with increasing scan rate. A sustained quasi-rectangular profile at higher sweep rates suggests an enhanced electrolyte ion diffusion throughout the mesoporous channels in the electrode materials.

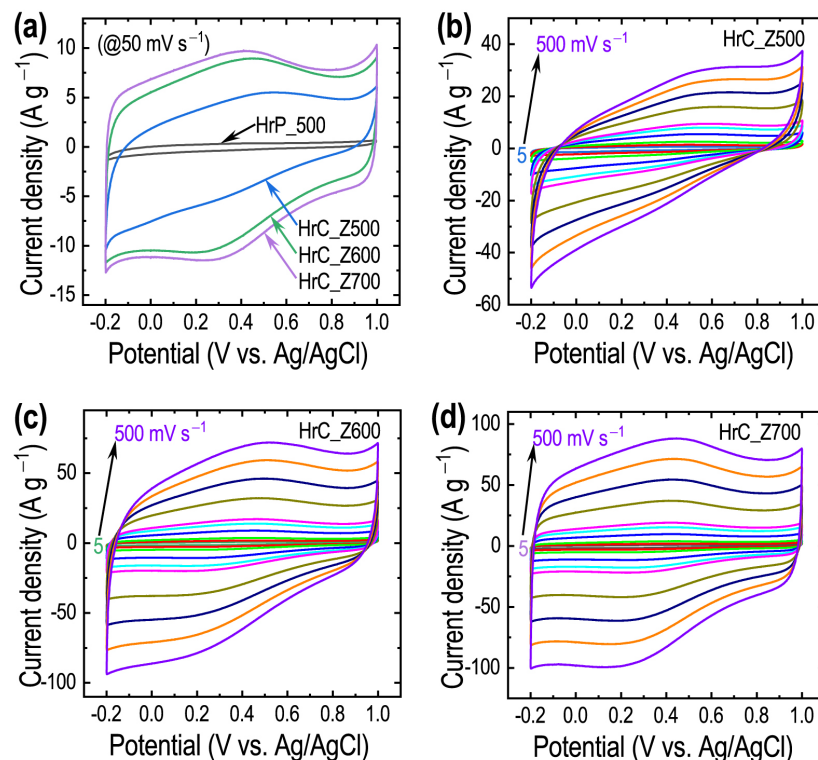


Figure 6. CV profiles of carbon materials derived from Harro. (a) CV response at a fixed scan rate of 50 mVs^{-1} , CV profiles at different scan rates (5 to 500 mVs^{-1}) for: (b) HrC_Z500, (c) HrC-Z600, and (d) HrC-Z700.

Electrochemical supercapacitance performance was also studied by GCD measurements. GCD responses were recorded over a wide range of current density, from 1 to 50 A g^{-1} . Figure 7a displays the GCD profiles for the electrodes at 1 A g^{-1} , where a triangular shape confirms the charge storage mechanism to EDLC-type [61–64]. In the GCD response, the discharge time, which measures the energy storage capacity of the electrode, depends on the surface textural properties. The GCD results show that the reference sample HrP_500 shows the shortest discharge time indicating a poor specific capacitance, which can be attributed to the lack of porosity, whereas HrC_Z700 has optimal surface area and porosity and gives the longest discharge time, confirming a maximum charge storage capacity based on its well-developed nanoporous structure. The specific capacitance (C_s) of HrC_Z700 calculated using Equation (1) at 1 A g^{-1} is 328.6 F g^{-1} , which is higher than that of other carbon materials derived from different biomass (Table S1) [12,14,16,33,36,39,65–88]. For other electrodes, values of C_s were calculated to be ca. 284.2 F g^{-1} (HrC_Z600), 203 F g^{-1} (HrC_Z500), and 9.3 F g^{-1} (HrP_500). These results demonstrate that the increase in carbonization temperature increases the porosity and surface area of the Harro carbon, and hence, there is an enhancement in the energy storage performance of the materials obtained at high temperature. The GCD curves of all the electrodes (Figure 7b and Figure S9a (HrC_Z700), S9b (HrP_500), S9c (HrC_Z500), and S9d (HrC_Z600)) have a persistent triangular shape even at 50 A g^{-1} (high current density), confirming prominent ion diffusion through the mesopores to the interiors of the electrodes.

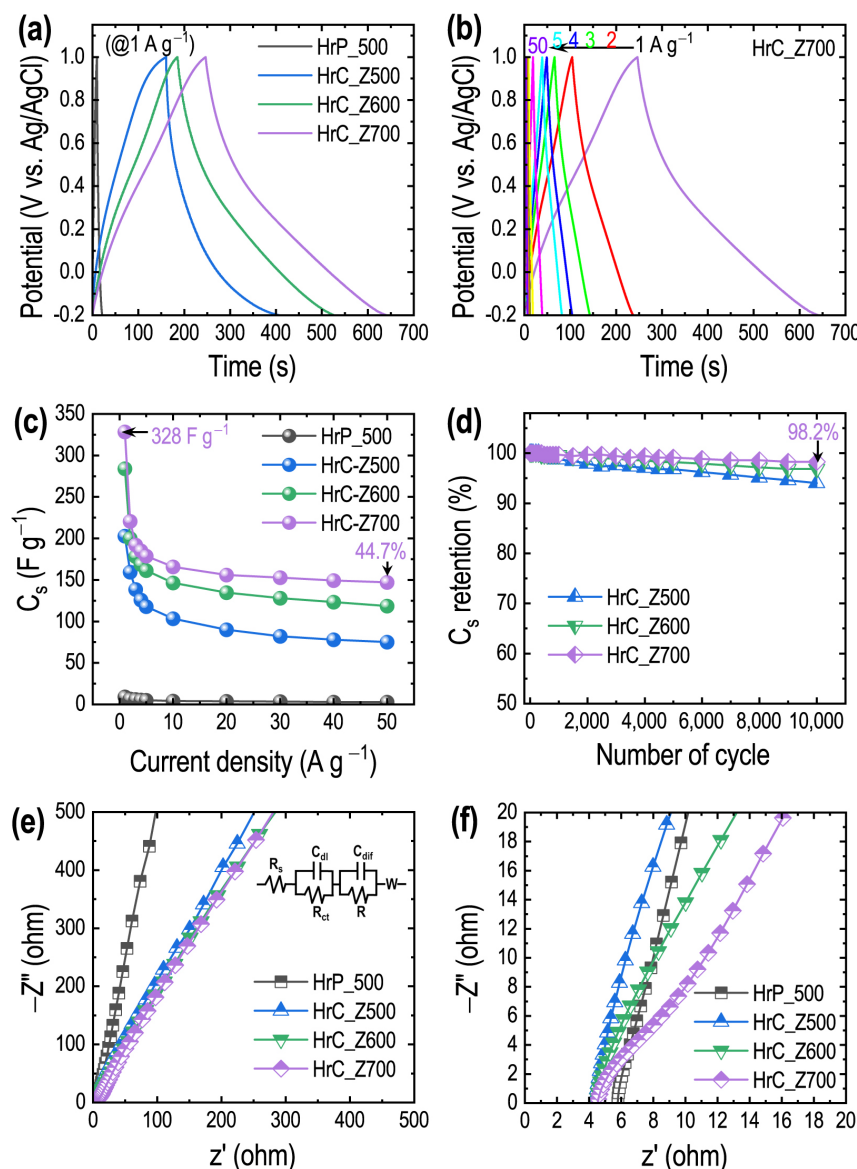


Figure 7. (a) Comparison of GCD profiles of the reference HrP_500 material and the ZnCl₂ activated carbon materials; HrC_Z500, HrC_Z600, and HrC_Z700 at 1 A g⁻¹; (b) GCD vs. current density profiles for the material with optimal textural properties (HrC_Z700); (c) calculated specific capacitance vs. current density profiles; (d) cycle performance of selected materials; (e) Nyquist plots recorded at 5 mV amplitude; and (f) the corresponding expanded plot. Inset of panel (e) represent equivalent circuit diagram. R_s , and R_{ct} represents electrolyte and charge transfer resistance, respectively. C_{dl} and R_{ct} refer to the double layer formation, and C_{dif} and R represent the diffusion contribution. W represent Warburg diffusion.

Figure 7c shows the calculated specific capacitance vs. current density plots. Note that the capacitance retention also increases with the increasing porosity and surface area of the electrode materials. The capacitance retention of the material having the optimal surface textural properties is ca. 44.7% at 50 A g⁻¹. Similarly, the cycle performance of the electrode is also correlated with the surface textural properties. The optimal sample has an outstanding cycle life of 98.2% after 10,000 consecutive charge/discharge cycles at 50 A g⁻¹. Figure 7e,f shows Nyquist plots that correlate electrolyte ions' diffusion kinetics, electron-transfer resistances, and double-layer charging at the electrode-electrolyte interface [89]. In the low-frequency region, the Nyquist plots have an approximately 45° gradient, suggesting the typical behavior of carbon materials with charge transfer resistance

and Warburg impedance (Figure 7e). A steep increase in the low-frequency region is due to rapid ion transfer to the electrode surface. The lack of a semicircular component in the high frequency region of the plots suggests ideal EDLC-type charge transfer properties (Figure 7f) [90,91]. The Nyquist plot was used to calculate the series resistance of the electrodes from the x-axis intercept of the imaginary component. It is ca. 5.7 Ω (HrP_500), 4.4 Ω (HrC_Z500), 4.5 Ω (HrC_Z600), and 4.5 Ω (HrC_Z700). The similarity in the values of series resistance confirms that the difference in the energy storage performance of these carbon materials is governed by the difference in the surface area and porosity.

The results obtained from the electrochemical measurements show that Harro seed stone biomass has considerable potential as a new inexpensive precursor for the production of carboniferous materials with hierarchically porous architectures, which are essential as the electrode materials for high-performance supercapacitor applications.

4. Conclusions

In summary, highly porous activated carbons were prepared from a new carbon source, *Terminalia chebula* (Harro) seed, by applying ZnCl_2 activation and different carbonization temperatures (400, 500, 600, and 700 $^\circ\text{C}$) under a nitrogen gas atmosphere. Chemical activation resulted in porous structures comprising both micro- and mesopore architectures. The carbon material obtained by carbonization at 700 $^\circ\text{C}$ displays optimal surface textural properties. Total specific surface area and pore volume are ca. 1382.6 $\text{m}^2 \text{g}^{-1}$ and 0.929 $\text{cm}^3 \text{g}^{-1}$, respectively. The sample performed well as an electrical double-layer capacitor electrode due to its large surface area and well-defined pore structure. This material exhibits good supercapacitance performance, giving a high specific capacitance of 328.6 F g^{-1} @ 1 A g^{-1} , accompanied by good a retention of capacitance of 44.7% at a large current density of 50 A g^{-1} with an outstanding cycle endurance at 98.2% after 10,000 charge/discharge cycles in an aqueous electrolyte solution (1 M H_2SO_4). Our results demonstrate that Harro seed stone has considerable potential as a low-cost source of carbon for the scale-up production of high-surface-area carbon materials with well-defined micro/mesopore structures required as electrode materials in high-performance energy storage supercapacitor applications.

Supplementary Materials: The following supporting information can be downloaded at: <https://www.mdpi.com/article/10.3390/c9040109/s1>, Figure S1: SEM images of HrP_500; Figure S2: SEM images of HrC_Z400; Figure S3: SEM images of HrC_Z500; Figure S4: SEM images of HrC_Z600; Figure S5: SEM images of HrC_Z700; Figure S6: TEM images of HrC_Z700; Figure S7: FTIR spectra of carbon materials; Figure S8: CV curves of HrP_500; Figure S9: Additional GCD data; Table S1: Comparison of the electrochemical supercapacitance performance of Harro seed stone-derived porous carbons with other carbon materials.

Author Contributions: Conceptualization, L.K.S.; methodology, L.K.S., C.L.G., R.M., M.P.A., R.R. and B.P.P.; validation, L.K.S., J.P.H. and K.A.; formal analysis, L.K.S., J.P.H. and R.M.; investigation, C.L.G., R.M. and L.K.S.; resources, L.K.S., R.R. and B.P.P.; data curation, L.K.S. and J.P.H.; writing—original draft preparation, C.L.G. and M.P.A.; writing—review and editing, L.K.S. and J.P.H.; visualization, L.K.S. and K.A.; supervision, L.K.S.; project administration, L.K.S., B.P.P. and K.A.; funding acquisition, L.K.S. and K.A. All authors have read and agreed to the published version of the manuscript.

Funding: This work was partially supported by JSPS KAKENHI Grant Numbers JP20H00392, JP20K05590, and JP23H05459.

Data Availability Statement: The data presented in this study are available upon request from the corresponding author.

Acknowledgments: C. L. Gnawali acknowledges the University Grant Commission (UGC), Nepal, for awarding research grants under the Ph.D. fellowship and Research Support (PhD-77/78-S&T-17) and thanks the Research Center for Materials Nanoarchitectonics (MANA), National Institute for Materials Science (NIMS), for the visiting researcher position from 29 August to 1 October 2022.

Conflicts of Interest: The authors declare no conflict of interest.

References

1. Kong, L.; Peng, H.-J.; Huang, J.-Q.; Zhang, Q. Advanced Energy Materials for Flexible Batteries in Energy Storage: A Review. *SmartMat* **2020**, *1*, e1007. [[CrossRef](#)]
2. Mahmud, S.; Rahman, M.; Kamurzzaman, M.; Ali, M.O.; Emon, M.S.A.; Khatun, H.; Ali, M.R. Recent Advances in Lithium-ion Battery Materials for Improved Electrochemical Performance: A review. *Results Eng.* **2022**, *15*, 100472. [[CrossRef](#)]
3. Jetybayeva, A.; Aaron, D.S.; Belharouak, I.; Mench, M.M. Critical Review on Recently Developed Lithium and Non-Lithium Anode-based Solid-State Lithium-ion Batteries. *J. Power Sources* **2023**, *566*, 232914. [[CrossRef](#)]
4. Simon, P.; Gogotsi, Y. Perspective for Electrochemical Capacitors and Related Devices. *Nat. Mater.* **2020**, *19*, 1151–1163. [[CrossRef](#)]
5. Qiao, Z.; Bian, K.; Ding, C.; Zhao, Y. Recent Progress of Carbon-Fiber-Based Electrode Materials for Energy Storage. *Diamond Relat. Mater.* **2023**, *138*, 110208. [[CrossRef](#)]
6. Pacchioni, G. Sustainable Flexible Supercapacitors. *Nat. Rev. Mater.* **2022**, *7*, 844. [[CrossRef](#)]
7. Wu, C.; Xing, X.; Xiong, W.; Li, H. Cooperative Regulation of Hard Template and Emulsion Self-Assembly to the Synthesis of N/O Co-doped Mesoporous Hollow Carbon Nanospheres for Supercapacitors. *Diamond Relat. Mater.* **2023**, *139*, 110273. [[CrossRef](#)]
8. Wang, F.; Wu, X.; Yuan, X.; Liu, Z.; Zhang, Y.; Fu, L.; Zhu, Y.; Zhou, Q.; Wu, Y.; Huang, W. Latest Advances in Supercapacitors: From New Electrode Materials to Novel Device Designs. *Chem. Soc. Rev.* **2017**, *46*, 6816–6854. [[CrossRef](#)]
9. Chatterjee, D.P.; Nandi, A.K. A Review on the Recent Advances in Hybrid Supercapacitors. *J. Mater. Chem. A* **2021**, *9*, 15880–15918. [[CrossRef](#)]
10. Shrestha, R.G.; Shrestha, L.K.; Ariga, K. Carbon Nanoarchitectonics for Energy Related Applications. *C J. Carbon Res.* **2021**, *7*, 73. [[CrossRef](#)]
11. Li, D.; Huang, Y.; Yu, C.; Tang, C.; Lin, J. Rapid Synthesis of Biomass-Derived Carbon via Induction Pyrolysis for Supercapacitors. *Diamond Relat. Mater.* **2023**, *136*, 109956. [[CrossRef](#)]
12. Gnawali, C.L.; Manandhar, S.; Shahi, S.; Shrestha, R.G.; Adhikari, M.P.; Rajbhandari, R.; Pokharel, B.P.; Ma, R.; Ariga, K.; Shrestha, L.K. Nanoporous Carbon Materials from Terminalia bellirica Seed for Methylene Blue Adsorption and High-Performance Supercapacitor Applications. *Bull. Chem. Soc. Jpn.* **2023**, *96*, 572–581. [[CrossRef](#)]
13. Shrestha, L.K.; Shrestha, R.G.; Chaudhary, R.; Pradhananga, R.R.; Tamrakar, B.M.; Shrestha, T.; Maji, S.; Shrestha, R.L.; Ariga, K. Nelumbo nucifera Seed-Derived Nitrogen-Doped Hierarchically Porous Carbons as Electrode Materials for High-Performance Supercapacitor Applications. *Nanomaterials* **2021**, *11*, 3175. [[CrossRef](#)] [[PubMed](#)]
14. Shrestha, R.G.; Maji, S.; Mallick, A.K.; Jha, A.; Shrestha, R.M.; Rajbhandari, R.; Hill, J.P.; Ariga, K.; Shrestha, L.K. Hierarchically Porous Carbon Materials from Phoenix Dactylifera Seed for High-Performance Supercapacitor Applications. *Bull. Chem. Soc. Jpn.* **2022**, *95*, 1060–1067. [[CrossRef](#)]
15. Shrestha, R.G.; Maji, S.; Shrestha, L.K.; Ariga, K. Nanoarchitectonics of Nanoporous Carbon Materials in Supercapacitors Applications. *Nanomaterials* **2020**, *10*, 639. [[CrossRef](#)]
16. Zhang, S.; Li, Y.; Du, Y.; Ma, X.; Lin, J.; Chen, S. Apple-Pomace-Based Porous Biochar as Electrode Materials for Supercapacitors. *Diamond Relat. Mater.* **2022**, *130*, 109507. [[CrossRef](#)]
17. Young, C.; Chen, H.-T. Supercapacitor Application of a Three-Dimensional Carbon Sphere–Intercalated Porous Carbon Fabricated Using a Hard Template and a Biomass Material. *Diamond Relat. Mater.* **2022**, *130*, 109528. [[CrossRef](#)]
18. Chang, P.; Cen, Y.; Li, X.; Zhang, C.; Li, L.; Luo, Y.; Dong, J.; Yang, T. Chitosan-Based 2D Highly Conductive Porous Carbon Nanosheet as Supercapacitor Electrode with High Voltage and Long Lifespan. *Diamond Relat. Mater.* **2022**, *130*, 109514. [[CrossRef](#)]
19. Xing, Z.; Zhang, L.; Pang, G.; Xu, J.; Wang, X.; Yang, C. High Performance Porous Carbon Derived from Platanus Leaves for a Solid-State Supercapacitor. *Diamond Relat. Mater.* **2021**, *120*, 108655. [[CrossRef](#)]
20. Karnan, M.; Subramani, K.; Sudhan, N.; Ilayaraja, N.; Sathish, M. Aloe Vera Derived Activated High-Surface-Area Carbon for Flexible and High-Energy Supercapacitors. *ACS Appl. Mater. Interfaces* **2016**, *8*, 35191–35202. [[CrossRef](#)]
21. Salanne, M.; Rotenberg, B.; Naoi, K.; Kaneko, K.; Taberna, P.L.; Grey, C.P.; Dunn, B.; Simon, P. Efficient Storage Mechanism for Building Better Supercapacitors. *Nat. Energy* **2016**, *1*, 16070. [[CrossRef](#)]
22. Jäckel, N.; Simon, P.; Gogotsi, Y.; Presser, V. Increase in Capacitance by Subnanometer Pores in Carbon. *ACS Energy Lett.* **2016**, *1*, 1262–1265. [[CrossRef](#)]
23. Zhu, Y.; Murali, S.; Stoller, M.D.; Ganesh, K.J.; Cai, W.; Ferreira, P.J.; Pirkle, A.; Wallace, R.M.; Cychosz, K.A.; Thommes, M.; et al. Carbon-based Supercapacitors Produced by Activation of Graphene. *Science* **2011**, *332*, 1537–1541. [[CrossRef](#)] [[PubMed](#)]
24. Tang, J.; Wang, J.; Shrestha, L.K.; Hossain, M.S.A.; Alothman, Z.A.; Yamauchi, Y.; Ariga, K. Activated Porous Carbon Spheres with Customized Mesopores through Assembly of Diblock Copolymers for Electrochemical Capacitor. *ACS Appl. Mater. Interface* **2017**, *9*, 18986–18993. [[CrossRef](#)]
25. Zhang, J.; Chen, Z.; Wang, G.; Hou, L.; Yuan, C. Eco-Friendly and Scalable Synthesis of Micro-/Mesoporous Carbon Sub-Microspheres as Competitive Electrodes for Supercapacitors and Sodium-Ion Batteries. *Appl. Surf. Sci.* **2020**, *533*, 147511. [[CrossRef](#)]
26. Luo, L.; Lan, Y.; Zhang, Q.; Deng, J.; Luo, L.; Zeng, Q.; Gao, H.; Zhao, W. A Review on Biomass-Derived Activated Carbon as Electrode Materials for Energy Storage Supercapacitors. *J. Energy Storage* **2022**, *55*, 105839. [[CrossRef](#)]

27. Manasa, P.; Sambasivam, S.; Ran, F. Recent Progress on Biomass Waste Derived Activated Carbon Electrode Materials for Supercapacitors Applications—A Review. *J. Energy Storage* **2022**, *54*, 105290. [[CrossRef](#)]
28. Liang, K.; Chen, Y.; Wang, D.; Wang, W.; Jia, S.; Mitsuzakic, N.; Chen, Z. Post-Modified Biomass Derived Carbon Materials for Energy Storage Supercapacitors: A Review. *Sustain. Energy Fuels* **2023**, *7*, 3541–3559. [[CrossRef](#)]
29. Raju, G.S.R.; Kondrat, S.; Chodankar, N.R.; Hwang, S.K.; Lee, J.H.; Long, T.; Pavitra, E.; Patil, S.J.; Ranjith, K.S.; Rao, M.V.B.; et al. Electrolyte Ions-Matching Hierarchically Porous Biochar Electrodes with an Extended Potential Window for Next-Generation Supercapacitors. *J. Mater. Chem. A* **2023**, *11*, 15540–15552. [[CrossRef](#)]
30. Maji, S.; Chaudhary, R.; Shrestha, R.G.; Shrestha, R.L.; Demir, B.; Searles, D.J.; Hill, J.P.; Yamauchi, Y.; Ariga, K.; Shrestha, L.K. High-Performance Supercapacitor Materials Based on Hierarchically Porous Carbons Derived from Artocarpus heterophyllum Seed. *ACS Appl. Energy Mater.* **2021**, *4*, 12257–12266. [[CrossRef](#)]
31. Ozpinar, P.; Dogan, C.; Demiral, H.; Morali, U.; Erol, S.; Samdan, C.; Yildiz, D.; Demiral, I. Activated Carbons Prepared from Hazelnut Shell Waste by Phosphoric Acid Activation for Supercapacitor Electrode Applications and Comprehensive Electrochemical Analysis. *Renew. Energy* **2022**, *189*, 535–548. [[CrossRef](#)]
32. Geng, Y.; Wang, J.; Wang, Q.; Chen, X.; Sun, S.; Zhang, S.; Tian, Y.; Liu, C.; Wang, L.; Wei, Z.; et al. N/O Co-Doped Hierarchical Nanoporous Biochar Derived from Waste Polypropylene Nonwoven for High-Performance Supercapacitors. *RSC Adv.* **2023**, *13*, 25877–25887. [[CrossRef](#)] [[PubMed](#)]
33. Prasankumar, T.; Salpekar, D.; Bhattacharya, S.; Manoharan, K.; Yadav, R.M.; Mata, M.A.C.; Miller, K.A.; Vajtai, R.; Jose, S.; Roy, S.; et al. Biomass Derived Hierarchical Porous Carbon for Supercapacitor Application and Dilute Stream CO₂ Capture. *Carbon* **2022**, *199*, 249–257. [[CrossRef](#)]
34. Sun, Y.; Xu, D.; Wang, S. Self-assembly of Biomass Derivatives into Multiple Heteroatom-Doped 3D-Interconnected Porous Carbon for Advanced Supercapacitors. *Carbon* **2022**, *199*, 258–267. [[CrossRef](#)]
35. Li, Y.; Zhang, D.; Zhang, Y.; He, J.; Wang, Y.; Wang, K.; Xu, Y.; Li, H.; Wang, Y. Biomass-Derived Microporous Carbon with Large Micropore Size for High-performance Supercapacitors. *J. Power Sources* **2020**, *448*, 227396. [[CrossRef](#)]
36. Zhang, G.; Bai, Q.; Wang, X.; Li, C.; Uyama, H.; Shen, Y. Preparation and Mechanism Investigation of Walnut Shell-Based Hierarchical Porous Carbon for Supercapacitors. *Bull. Chem. Soc. Jpn.* **2023**, *96*, 190–197. [[CrossRef](#)]
37. Shrestha, L.K.; Shahi, S.; Gnawali, C.L.; Adhikari, M.P.; Rajbhandari, R.; Pokharel, B.P.; Ma, R.; Shrestha, R.G.; Ariga, K. Phyllanthus emblica Seed-Derived Hierarchically Porous Carbon Materials for High-Performance Supercapacitor Applications. *Materials* **2022**, *15*, 8335. [[CrossRef](#)]
38. Xu, Q.; Ni, X.; Chen, S.; Ye, J.; Yang, J.; Wang, H.; Li, D.; Yuan, H. Hierarchically Porous Carbon from Biomass Tar as Sustainable Electrode Material for High-Performance Supercapacitors. *Int. J. Hydrog. Energy* **2023**, *48*, 25635–25644. [[CrossRef](#)]
39. Liu, H.; Chen, W.; Zhang, R.; Ren, Y. Naturally O-N-S Co-Doped Carbon with Multiscale Pore Architecture Derived from Lotus Leaf Stem for High-Performance Supercapacitors. *Bull. Chem. Soc. Jpn.* **2021**, *94*, 1705–1714. [[CrossRef](#)]
40. Zhen, L.-H.; Chen, M.-H.; Liang, S.-X.; Lü, Q.-F. Oxygen-Rich Hierarchical Porous Carbon Derived from Biomass Waste-Kapok Flower for Supercapacitor Electrode. *Diamond Relat. Mater.* **2021**, *113*, 108267. [[CrossRef](#)]
41. Qiao, Y.; Zhang, R.; Li, R.; Fang, W.; Cui, Z.; Zhang, D. Green Synthesis of Hierarchical Porous Carbon with Adjustable Porosity for High Performance Supercapacitors. *Diamond Relat. Mater.* **2021**, *117*, 108488. [[CrossRef](#)]
42. Yeleuov, M.; Daulbayev, C.; Taurbekov, A.; Abdisttar, A.; Ebrahim, R.; Kumekov, S.; Prikhodko, N.; Lesbayev, B.; Batyrzhan, K. Synthesis of Graphene-like Porous Carbon from Biomass for Electrochemical Energy Storage Applications. *Diamond Relat. Mater.* **2021**, *119*, 108560. [[CrossRef](#)]
43. Phukhrongthung, A.; Iamprasertkun, P.; Bunpheng, A.; Saisopa, T.; Umpuch, C.; Puchongkawarin, C.; Sawangphruk, M.; Luanwuthi, S. Oil Palm Leaf-Derived Hierarchical Porous Carbon for “Water-in-Salt” Based Supercapacitors: The Effect of Anions (Cl[−] and TFSI[−]) in Superconcentrated Conditions. *RSC Adv.* **2023**, *13*, 24432–24444. [[CrossRef](#)] [[PubMed](#)]
44. Lima, R.M.A.P.; dos Reis, G.S.; Lassi, U.; Lima, E.C.; Dotto, G.L.; de Oliveira, H.P. Sustainable Supercapacitors Based on Polypyrrole-Doped Activated Biochar from Wood Waste Electrodes. *C J. Carbon Res.* **2023**, *9*, 59. [[CrossRef](#)]
45. Lv, T.; Li, J.; Shi, Y.; Yu, H.; Chen, J. Activating Biomass Carbon with Metallurgical Slag by Pyrolysis in Molten Salt for High-Performance Supercapacitors. *RSC Adv.* **2023**, *13*, 23021–23029. [[CrossRef](#)]
46. Escalante, J.; Chen, W.-H.; Tabatabaei, M.; Hoang, A.T.; Kwon, E.E.; Lin, K.-Y.A.; Saravanakumar, A. Pyrolysis of Lignocellulosic, Algal, Plastic, and Other Biomass Wastes for Biofuel Production and Circular Bioeconomy: A Review of Thermogravimetric Analysis (TGA) Approach. *Renew. Sustain. Energy Rev.* **2022**, *169*, 112914. [[CrossRef](#)]
47. Geng, X.; Singh, G.; Sathish, C.I.; Li, Z.; Bahadur, R.; Liu, Y.; Li, S.; Yu, X.; Breese, M.; Yi, J.; et al. Biomass Derived Nanoarchitectonics of Porous Carbon with Tunable Oxygen Functionalities and Hierarchical Structures and their Superior Performance in CO₂ Adsorption and Energy Storage. *Carbon* **2023**, *214*, 118347. [[CrossRef](#)]
48. Singh, G.; Bahadur, R.; Ruban, A.M.; Davidraj, J.M.; Su, D.; Vinu, A. Synthesis of Functionalized Nanoporous Biocarbons with High Surface Area for CO₂ Capture and Supercapacitor Applications. *Green Chem.* **2021**, *23*, 5571–5583. [[CrossRef](#)]
49. Ghahremani, P.; Mostafatabar, A.H.; Bahlakeh, G.; Ramezanzadeh, B. Rational Design of a Novel Multi-Functional Carbon-Based Nano-Carrier Based on Multi-Walled-CNT-Oxide/Polydopamine/Chitosan for Epoxy Composite with Robust pH-Sensitive Active Anti-Corrosion Properties. *Carbon* **2022**, *189*, 113–141. [[CrossRef](#)]

50. Ouyang, J.; Wang, X.; Wang, L.; Xiong, W.; Li, M.; Hua, Z.; Zhao, L.; Zhou, C.; Liu, X.; Chen, H.; et al. Construction of a Porous Carbon Skeleton in Wood Tracheids to Enhance Charge Storage for High-Performance Supercapacitors. *Carbon* **2022**, *196*, 532–539. [[CrossRef](#)]
51. Kruk, M.; Jaroniec, M. Gas Adsorption Characterization of Ordered Organic–Inorganic Nanocomposite Materials. *Chem. Mater.* **2001**, *13*, 3169–3183. [[CrossRef](#)]
52. Sing, K. The Use of Nitrogen Adsorption for the Characterisation of Porous Materials. *Colloid Surf. A* **2001**, *187–188*, 3–9. [[CrossRef](#)]
53. Ahammad, A.J.S.; Odhikari, N.; Shah, S.S.; Hasan, M.M.; Islam, T.; Pal, P.R.; Qasem, M.A.A.; Aziz, M.A. Porous Tal Palm Carbon Nanosheets: Preparation, Characterization and Application for the Simultaneous Determination of Dopamine and Uric Acid. *Nanoscale Adv.* **2019**, *1*, 613–626. [[CrossRef](#)] [[PubMed](#)]
54. Gan, Y.X. Activated Carbon from Biomass Sustainable Sources. *C J. Carbon Res.* **2021**, *7*, 39. [[CrossRef](#)]
55. Bejjanki, D.; Banothu, P.; Kumar, V.B.; Kumar, P.S. Biomass-Derived N-Doped Activated Carbon from *Eucalyptus* Leaves as an Efficient Supercapacitor Electrode Material. *C J. Carbon Res.* **2023**, *9*, 24. [[CrossRef](#)]
56. Baskar, A.V.; Ruban, A.M.; Davidraj, J.M.; Singh, G.; Al-Muhtaseb, A.H.; Lee, J.M.; Yi, J.; Vinu, A. Single-Step Synthesis of 2D Mesoporous C₆₀/Carbon Hybrids for Supercapacitor and Li-Ion Battery Applications. *Bull. Chem. Soc. Jpn.* **2021**, *94*, 133–140. [[CrossRef](#)]
57. Harris, P.J.F. New Perspective on the Structure of Graphitic Carbons. *Crit. Rev. Solid State Mater. Sci.* **2005**, *30*, 235–253. [[CrossRef](#)]
58. Lee, S.-M.; Lee, S.-H.; Roh, J.-S. Analysis of Activation Process of Carbon Black Based on Structural Parameters Obtained by XRD Analysis. *Crystals* **2021**, *11*, 153. [[CrossRef](#)]
59. Shrestha, L.K.; Adhikari, L.; Shrestha, R.G.; Adhikari, M.P.; Adhikari, R.; Hill, J.P.; Pradhananga, R.R.; Ariga, K. Nanoporous Carbon Materials with Enhanced Supercapacitance Performance and Non-Aromatic Chemical Sensing with C1/C2 Alcohol Discrimination. *Sci. Technol. Adv. Mater.* **2016**, *17*, 483–492. [[CrossRef](#)]
60. Zavidovskiy, I.A.; Streletskiy, O.A.; Nuriahmetov, I.F.; Nishchak, O.Y.; Savchenko, N.F.; Tatarintsev, A.A.; Pavlikov, A.V. Highly Selective Polyene-Polyyne Resistive Gas Sensors: Response Tuning by Low-Energy Ion Irradiation. *J. Compos. Sci.* **2023**, *7*, 156. [[CrossRef](#)]
61. Miller, J.R.; Simon, P. Materials Science-Electrochemical Capacitors for Energy, Management. *Science* **2008**, *321*, 651–652. [[CrossRef](#)] [[PubMed](#)]
62. Yang, Z.; Ren, J.; Zhang, Z.; Chen, X.; Guan, G.; Qiu, L.; Zhang, Y.; Peng, H. Recent Advancement of Nanostructured Carbon for Energy Applications. *Chem. Rev.* **2015**, *115*, 5159–5223. [[CrossRef](#)] [[PubMed](#)]
63. Huang, J.; Zhao, B.; Liu, T.; Mou, J.; Jiang, Z.; Liu, J.; Li, H.; Liu, M. Wood-Derived Materials for Advanced Electrochemical Energy Storage Devices. *Adv. Funct. Mater.* **2019**, *29*, 1902255. [[CrossRef](#)]
64. Chang, P.; Zhang, J.; Cen, Y.; Yang, F.; Li, X.; Xie, Q.; Dong, J. 3D Hierarchical Porous Carbon from Fulvic Acid Biomass for High Energy Density Supercapacitor with High Withstanding Voltage. *J. Power Sources* **2022**, *533*, 231413. [[CrossRef](#)]
65. Lobato-peralta, D.R.; Duque-Brito, E.; Orugba, H.O.; Arias, D.M.; Cuentas-Gallegos, A.K.; Okolie, J.A.; Okoye, P.U. Sponge-like Nanoporous Activated Carbon from Corn Husk as a Sustainable and Highly Stable Supercapacitor Electrode for Energy Storage. *Diamond Relat. Mater.* **2023**, *138*, 110176. [[CrossRef](#)]
66. Tu, J.; Qiao, Z.; Wang, Y.; Li, G.; Zhang, X.; Li, G.; Ruan, D. American Ginseng Biowaste-Derived Activated Carbon for High-Performance Supercapacitors. *Intl. J. Electrochem. Sci.* **2023**, *18*, 16–24. [[CrossRef](#)]
67. Wang, J.; Zhang, Q.; Deng, M. Eco-Friendly Preparation of Biomass-Derived Porous Carbon and its Electrochemical Properties. *ACS Omega* **2022**, *7*, 22689–22697. [[CrossRef](#)]
68. Wang, J.; Yang, H.; Feng, Y.; Gao, X.; Zhou, C.; Cong, S.; Ke, S. High-performance Supercapacitor Electrodes from Porous Rotten Wood Cellulose-derived Carbon via Fungi Action. *Chem. Lett.* **2023**, *52*, 389–392. [[CrossRef](#)]
69. Shrestha, R.L.; Chaudhary, R.; Shrestha, T.; Tamrakar, B.M.; Shrestha, R.G.; Maji, S.; Hill, J.P.; Ariga, K.; Shrestha, L.K. Nanoarchitectonics of Lotus Seed Derived Nanoporous Carbon Materials for Supercapacitor Applications. *Materials* **2020**, *13*, 5434. [[CrossRef](#)]
70. Shrestha, R.L.; Chaudhary, R.; Shrestha, R.G.; Shrestha, T.; Maji, S.; Ariga, K.; Shrestha, L.K. Washnut Seed-Derived Ultrahigh Surface Area Nanoporous Carbons as High Rate Performance Electrode Material for Supercapacitors. *Bull. Chem. Soc. Jpn.* **2021**, *94*, 565–572. [[CrossRef](#)]
71. Shrestha, R.L.; Shrestha, T.; Tamrakar, B.M.; Shrestha, R.G.; Maji, S.; Ariga, K.; Shrestha, L.K. Nanoporous Carbon Materials Derived from Washnut Seed with Enhanced Supercapacitance. *Materials* **2020**, *13*, 2371. [[CrossRef](#)]
72. Chaudhary, R.; Maji, S.; Shrestha, R.G.; Shrestha, R.L.; Shrestha, T.; Ariga, K.; Shrestha, L.K. Jackfruit Seed-Derived Nanoporous Carbons as the Electrode Material for Supercapacitors. *C J. Carbon Res.* **2020**, *6*, 73. [[CrossRef](#)]
73. Gao, F.; Zhang, J.; Ren, M.; Ge, Y.; Chen, H.; Ma, X.; Hao, Q. Preparation and Characterization of Porous Carbons by Pyrolysis-CO₂ Gasification of Pine Sawdust. *Chem. Lett.* **2020**, *49*, 652–655. [[CrossRef](#)]
74. Gehrke, V.; Maron, G.K.; Rodrigues, L.D.S.; Alano, J.H.; Pereira, C.M.P.D.; Orlandi, M.O.; Carreño, N.L.V. Facile Preparation of a Novel Biomass-Derived H₃PO₄ and Mn(NO₃)₂ Activated Carbon from Citrus Bergamia Peels for High-Performance Supercapacitors. *Mater. Today Commun.* **2021**, *26*, 101779. [[CrossRef](#)]
75. Selvaraj, A.R.; Muthusamy, A.; Cho, I.; Kim, H.-J.; Senthil, K.; Prabakar, K. Ultrahigh Surface Area Biomass Derived 3D Hierarchical Porous Carbon Nanosheet Electrodes for High Energy density Supercapacitors. *Carbon* **2021**, *174*, 463. [[CrossRef](#)]

76. Shrestha, L.K.; Shrestha, R.G.; Maji, S.; Pokharel, B.P.; Rajbhandari, R.; Shrestha, R.L.; Pradhananga, R.R.; Hill, J.P.; Ariga, K. High Surface Area Nanoporous Graphitic Carbon Materials Derived from Lapsi Seed with Enhanced Supercapacitance. *Nanomaterials* **2020**, *10*, 728. [[CrossRef](#)] [[PubMed](#)]
77. Song, Y.; Qu, W.; He, Y.; Yang, H.; Du, M.; Wang, A.; Yang, Q.; Chen, Y.Q. Synthesis and Processing Optimization of N-doped Hierarchical Porous Carbon Derived from Corncob for High Performance Supercapacitors. *J. Energy Storage* **2020**, *32*, 101877. [[CrossRef](#)]
78. Liu, Y.; Shi, Z.; Gao, Y.; An, W.; Cao, Z.; Liu, J. Biomass-Swelling Assisted Synthesis of Hierarchical Porous Carbon Fibers for Supercapacitor Electrodes. *ACS Appl. Mater. Interfaces* **2016**, *8*, 28283–28290. [[CrossRef](#)]
79. Jiang, Y.; Zhang, Z.; Zhang, Y.; Zhou, X.; Wang, L.; Yasin, A.; Zhang, L. Bioresource Derived Porous Carbon from Cottonseed Husk for Removal of Triclosan and Electrochemical Application. *RSC Adv.* **2018**, *8*, 42405–42414. [[CrossRef](#)]
80. Zhu, Y.; Chen, M.; Zhang, Y.; Zhao, W.; Wang, C. A Biomass-Derived Nitrogen-doped Porous Carbon for High-Energy Supercapacitor. *Carbon* **2018**, *140*, 404–412. [[CrossRef](#)]
81. Lu, T.; Xu, X.; Zhang, S.; Pan, L.; Wang, Y.; Alshehri, S.M.; Ahamad, T.; Kim, M.; Na, J.; Hossain, M.S.A.; et al. High-Performance Capacitive Deionization by Lignocellulose-Derived Eco-Friendly Porous Carbon Materials. *Bull. Chem. Soc. Jpn.* **2020**, *93*, 1014–1019. [[CrossRef](#)]
82. Cao, M.; Wang, Q.; Cheng, W.; Huan, S.; Hu, Y.; Niu, Z.; Han, G.; Cheng, H.; Wang, G. A Novel Strategy Combining Electrospraying and One-Step Carbonization for the Preparation of Ultralight Honeycomb-Like Multilayered Carbon from Biomass-Derived Lignin. *Carbon* **2021**, *179*, 68–79. [[CrossRef](#)]
83. Schlee, P.; Hosseinaei, O.; Baker, D.; Landmér, A.; Tomani, P.; Mostazo-López, M.J.; Cazorla-Amorós, D.; Herou, S.; Titirici, M.-M. From Waste to Wealth: From Kraft Lignin to Free-Standing Supercapacitors. *Carbon* **2019**, *145*, 470–480. [[CrossRef](#)]
84. Liu, B.; Yang, M.; Chen, H.; Liu, Y.; Yang, D.; Li, H. Graphene-Like Porous Carbon Nanosheets Derived from *Salvia splendens* for High-Rate Performance Supercapacitors. *J. Power Sources* **2018**, *397*, 1–10. [[CrossRef](#)]
85. Tian, Y.; Ren, Q.; Chen, X.; Li, L.; Lan, X. Yeast-Based Porous Carbon with Superior Electrochemical Properties. *ACS Omega* **2022**, *7*, 654–660. [[CrossRef](#)] [[PubMed](#)]
86. Huang, Y.; Peng, L.; Liu, Y.; Zhao, G.; Chen, J.Y.; Yu, G. Biobased Nano Porous Active Carbon Fibers for High-Performance Supercapacitors. *ACS Appl. Mater. Interface* **2016**, *8*, 15205–15215. [[CrossRef](#)]
87. Chen, Z.; Zhou, H.; Hu, Y.; Lai, H.; Liu, L.; Zhong, L.; Peng, X. Wood-Derived Lightweight and Elastic Carbon Aerogel for Pressure Sensing and Energy Storage. *Adv. Funct. Mater.* **2020**, *30*, 1910292. [[CrossRef](#)]
88. Shang, Z.; An, X.; Zhang, H.; Shen, M.; Baker, F.; Liu, Y.; Liu, L.; Yang, J.; Cao, H.; Xu, Q.; et al. Houttuynia-Derived Nitrogen-Doped Hierarchically Porous Carbon for High-Performance Supercapacitor. *Carbon* **2020**, *161*, 62–70. [[CrossRef](#)]
89. Mei, B.-A.; Munteshari, O.; Lau, J.; Dunn, B.; Pilon, L. Physical Interpretations of Nyquist Plots for EDLC Electrodes and Devices. *J. Phys. Chem. C* **2018**, *122*, 194–206. [[CrossRef](#)]
90. Eftekhari, A. The Mechanism of Ultrafast Supercapacitors. *J. Mater. Chem. A* **2018**, *6*, 2866–2876. [[CrossRef](#)]
91. Lee, K.-C.; Lim, M.S.W.; Hong, Z.-Y.; Chong, S.; Tiong, T.J.; Pan, G.-T.; Huang, C.-M. Coconut Shell-Derived Activated Carbon for High-Performance Solid-State Supercapacitors. *Energies* **2021**, *14*, 4546. [[CrossRef](#)]

Disclaimer/Publisher’s Note: The statements, opinions and data contained in all publications are solely those of the individual author(s) and contributor(s) and not of MDPI and/or the editor(s). MDPI and/or the editor(s) disclaim responsibility for any injury to people or property resulting from any ideas, methods, instructions or products referred to in the content.